
COMPLIANT ACTUATORS THAT MIMIC BIOLOGICAL MUSCLE PERFORMANCE WITH APPLICATIONS IN A HIGHLY BIOMIMETIC ROBOTIC ARM

Haosen Yang

The Department of Mechanical, Aerospace and Civil Engineering
University of Manchester
Manchester, M13 9PL, UK
haosen.yang@postgrad.manchester.ac.uk

Guowu Wei

School of Science, Engineering and Environment
University of Salford
Salford, M5 4WT, UK
g.wei@salford.ac.uk

Lei Ren

The Key Laboratory of Bionic Engineering, Ministry of Education
Jilin University
Changchun 130025, China
lren@jlu.edu.cn

Lingyun Yan

Department of Robotics Engineering, School of Electrical and Electronic Engineering
Shanghai Institute of Technology
Shanghai, 200235, China
lingyunyan@sit.edu.cn

November 1, 2023

ABSTRACT

This paper endeavours to bridge the existing gap in muscular actuator design for ligament-skeletal-inspired robots, thereby fostering the evolution of these robotic systems. We introduce two novel compliant actuators, namely the Internal Torsion Spring Compliant Actuator (ICA) and the External Spring Compliant Actuator (ECA), and present a comparative analysis against the previously conceived Magnet Integrated Soft Actuator (MISA) through computational and experimental results. These actuators, employing a motor-tendon system, emulate biological muscle-like forms, enhancing artificial muscle technology. A robotic arm application inspired by the skeletal ligament system is presented. Experiments demonstrate satisfactory power in tasks like lifting dumbbells (peak power: 36W), playing table tennis (end-effector speed: 3.2 m/s), and door opening, without compromising biomimetic aesthetics. Compared to other linear stiffness serial elastic actuators (SEAs), ECA and ICA exhibit high power-to-volume ($361 \times 10^3 \text{ W/m}^3$) and power-to-mass (111.6 W/kg) ratios respectively, endorsing the biomimetic design's promise in robotic development.

Keywords Artificial muscle, compact compliant actuator, series elastic actuator, biomimetic robots.

1 Introduction

The escalating integration of robots and humans in intricate environments accentuates the imperative of flexibility and safety in design. Two prevalent methodologies, algorithmic and mechanical compliance, are employed to fortify safety in robotic systems. Algorithmic compliance maintains rigidity in robots while modulating joint torque [1], albeit susceptible to sensor data inaccuracies, necessitating recalibration in divergent environments. Conversely, mechanical compliance enhances safety by absorbing unforeseen impacts, even sans power [2]. Pratt et al. [3] made the first proposal for a Series Elastic Actuator (SEA) to achieve mechanical compliance through the utilization of an elastic element that provides compliant coupling between the geared motor and the end effector [2], followed by the advent of Variable Stiffness Actuators (VSA) that mimic biological muscle attributes, finding utility in soft and exoskeleton robotics [4–8]. These technological incorporations propel robotic systems towards enhanced safety and flexibility.

While rotational SEA and VSA discussed above which are based on the hinge-joint design scheme may be effective for providing compliance in industrial and traditional robots [9–14], they are not well-suited in the development of a highly biomimetic robot. Tendon-driven actuation, essential for enhanced biomimicry, desires an actuator emulating biological muscle. This technique endows actuators with muscle-like appearance and functionality [15–17]. Tendon-driven robots employ electronic motors, positioned either remotely or locally [18, 19]. However, in most tendon-driven robotic limb and assistive exoskeletons designs combined with SEAs or VSAs [20–27], the motors are positioned remotely to allow the use of large motors. This configuration may cause considerable frictional challenges, and decrease the precision of joint movements and the effectiveness of joint torque. A more desirable design is a local tendon-driven scheme combined with either SEAs or VSAs. By utilizing this approach, the actuator can be situated closer to the joint, which allows for better emulation of the properties of biological muscles and avoids the interactions caused by tendons crossing multiple joints. This approach can lead to improved performance and more natural movements for robotic systems designed to mimic human motion.

This paper presents two innovative compact motor-based, muscle-like actuators employing a local tendon-driven mechanism and benefiting from SEA designs. The elastic elements in these actuators differ—being linear as seen in compression and torsion springs. Each actuator exhibits advantages and limitations regarding compactness and speed. A comparison is drawn with a prior design, MISA [28], which utilizes non-linear stiffness elastic elements like oppositely placed magnets. The suitability of each actuator varies across application scenarios, and a thorough analysis delineates the trade-offs, guiding researchers and engineers in choosing the right actuator for their applications, thereby informing future robotic design endeavours.

2 Related work

2.1 Motor-based compliant actuators

The Hill-based model from the 1930s is a widely accepted representation of human muscle [29]. It consists of three key components: the parallel element (PE), the series element (SE), and the contractile element (CE). The PE represents the mechanical properties of the muscle fibre membrane, muscle fascia and other connective tissue when the muscle is relaxed. The SE represents the inherent elasticity of the muscle fibres, and the CE represents the muscle fibres themselves. Based on this model, researchers have proposed SEAs which add a series elements with constant elasticity and damping to decouple the motor (CE) from the end effector, so that the output force of the SEA corresponds to its deformation. SEAs are widely used in a variety of applications, including exoskeleton robots [22, 30–34], lower limb robots [35–39], prosthetics [40–42], humanoid robots [43], rehabilitation robots [44, 45] and other areas.

The most conventional SEAs are rotary, linear, and tendon-driven. Rotary SEAs add linear stiffness elastic elements, such as torsion springs, between the motors and the driven joints [46, 47]. These actuators are typically placed at the joint and drive the joint directly, which may increase the size of the robot joint. Linear SEAs add extension springs between linear actuators and the driven arms [48, 49] which are usually longer in length. For SEAs combined with tendon-driven methods, series extension springs [42] are widely used, or torsion springs are added between motors and the driving pulleys [50]. However, these SEAs are usually used for remote tendon-driven joints, which are not designed to be muscle-shaped and therefore difficult to implement in highly biomimetic robots.

Magid & Law investigated the length-tension relationship of the frog muscle [51] in 1895. It shows the non-linear property, where the curve slope increases as the length increases. To emulate the biologic muscle properties, VSA was developed. A Non-linear elastic element or a stiffness adjustable device were used to represent the SEs in the Hill-based model [52–59]. Similar to SEAs, VSAs can be classified as rotary and tendon-driven types. Typical rotary VSAs use linear springs sets [24, 55, 60, 61], elastomer-based material [62], or non-linear stiffness torsion springs [38, 63, 64]. The joints are driven by the rotary VSAs directly, with the elastic elements placed between the driven joints and the motors. For VSAs with tendon-driven joints, spring-pulley systems are normally used [8, 32, 65], which allow the VSAs to be

capable of achieving an infinite range of joint stiffness. Another commonly used mechanism is connecting tendons to the driven joint via a non-linear spring [25]. Compared to linear stiffness SEAs, robot joints equipped with VSAs are able to present softer joints when receiving a small external force. When the impact force dramatically increases, the joint stiffness increases accordingly.

Most current SEAs and VSAs are intended for applications where the joints are driven directly by motors or remotely by motors through the tendon. For rotary compliant actuators at joints where the motor shaft and joint rotation axis coincide, the integration of motors, gearboxes, and soft elements at the joints usually results in oversized joints compared to biological joints. For current SEAs and VSAs integrated tendon-driven schemes, due to the use of remote-driven design, these actuators require large support systems including motor support and tendon guidance systems. They abandoned muscle-like shapes, making it difficult to achieve a human-like form in the serving robots. In addition, the tendon-driven method can be challenged by the requirement to drive a joint through multiple joints. For example, to drive the elbow joint, a motor placed in the torso may require a tendon passing through the shoulder joint, resulting in interactions between joint actuation. Additionally, the employment of extended tendons may cause considerable frictional challenges. The stretching of tendons and their ensuing durability constitute concerns, thereby decreasing the precision of joint movements. A guiding tube is required to direct the tendon to the driven joint. This may limit the tensile force transmitted by the tendon, thereby restricting the joint's torque output.

Optimizing motor-based compliant actuators for local tendon-driven artificial muscles with muscle-like shapes and properties is an innovative design direction. These actuators must be compact, lightweight, and possess high performance, including a high power-to-volume ratio, high power-to-mass ratio, large elastic travel, and a wide range of stiffness variation for VSA. However, designing motor-based artificial muscles that can be applied to various joints without modification is challenging. Unlike the remote control scheme that allows for large-size motors and complicated soft components, this new design direction requires minimizing size and weight while maintaining a muscle-like shape. Therefore, it remains to be determined whether actuators based on this design concept can drive highly biomimetic biological robots with high output capacity. Further research and development in this direction may be necessary to address these challenges and explore the potential for local tendon-driven artificial muscles to drive highly biomimetic robots.

2.2 Biomimetic robots

For decades, robots have predominantly utilized geared motors for joint actuation, directly connecting motors to hinge or universal joints. Notable instances of such designs encompass the Robotic arm and hand system [11], BHR-5 robot [10], ASIMO robot [66], WABIAN-2 robot [67], THBIP-2 robot [68], Phoenix robot [69], and Tesla robot [70]. These systems, while offering merits like streamlined design, ease of maintenance, cost-efficiency, and precise movement, diverge fundamentally from human biomechanics. Key limitations include the vulnerability of high-torque motors and their reduction gear systems to sudden impacts, risking damage. Such vulnerabilities raise safety concerns, especially in human-robot interaction contexts. Additionally, the cascading of single-DOF joints to achieve multi-DOF configurations often necessitates increased spatial allocations, thereby constraining operational versatility.

A paradigm shift towards highly biomimetic robots is evident in contemporary robotics. These robots emulate human musculoskeletal architectures, encompassing bones, joints, and musculature. They leverage tendon-driven mechanisms, inspired by human joints, to foster human-analogous kinematics and aesthetics. Pioneering in this arena are models like the Kenshiro robot [17], Kojiro robot [15], ECCE [16], and Roboy [26] which may employ ligaments for joint stabilization. However, a critique emerges in their often-overly simplified replication of human anatomy. While striving for functional equivalence, they sometimes neglect essential soft components. Instead of artificial muscles, many employ motors positioned remotely, actuating joints via tendons, which might introduce disparities in form and size relative to human counterparts. Central to advancing such robots is the evolution of artificial muscle designs. Researchers have innovated diverse artificial muscle variants, including pneumatic muscles [65] and twisted and coiled fibers [71]. These actuators, characterized by inherent compliance, can be tailored for specific applications. Nonetheless, challenges persist: some variants, which depend on thermal contractions, confront issues with precise control and rapid cooling, making motor-based soft artificial muscles a prevalent choice.

This paper seeks to bridge the existing gap, presenting a comparative analysis of three motor-based muscle-like actuators, amalgamating local-tendon-driven modalities with SEA and VSA designs.

3 Design and characteristics of compliant actuators

To address the problem listed above, this section introduces the design of two tendon-driven compliant actuators that can achieve various degrees of bionic properties. Fig. 1 shows the design schematic diagrams and CAD models of these

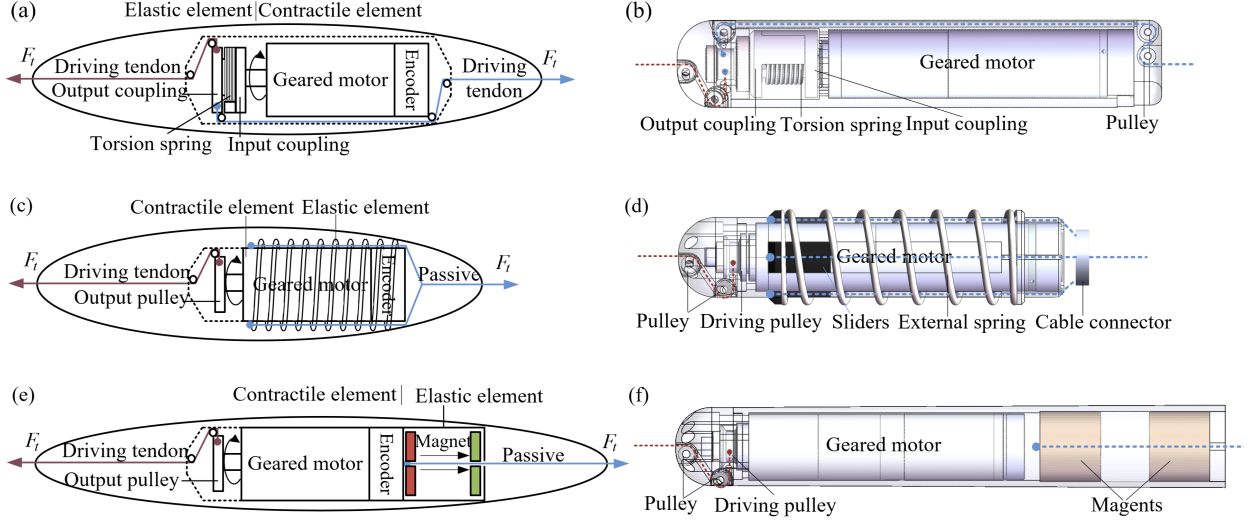


Figure 1: Schematic diagrams and CAD models of three compliant actuators, including (a) (b) Internal Linear Torsion Spring Compliant Actuator (ICA); (c) (d) External Linear Spring Coft Actuator (ECA); (e) (f) Magnet Integrated Non-linear Soft Actuator (MISA) [28].

actuators including the Internal Linear Spring Compliant Actuator (ICA) (Fig. 1(a) and (b)), the External Linear Spring Compliant Actuator (ECA) (Fig. 1(c) and (d)), and the previous introduced Magnets Integrated Non-linear Compliant Actuator (MISA) (Fig. 1(e) and (f)) [28]. For a comprehensive elucidation on the design of the MISA, we direct the reader to our preceding work.

3.1 Internal Spring Compliant Actuator (ICA)

In biomimetic robots, artificial muscles typically adopt an elongated configuration, as exemplified by pneumatic and hydraulic muscles. When designing artificial muscles using brushless motors, the rated power of the motor is intrinsically linked to its size. This poses a challenge: integrating a high-power motor while maintaining compact dimensions is pivotal, especially for upper limb robots. The actuators presented herein are designed with this constraint in mind, prioritizing compactness by limiting the outer diameter. The inaugural actuator ensures an outer diameter only 13.6% greater than the motor diameter. Compliance is ingeniously introduced by interposing a torsion spring between the motor and output pulley.

Fig. 1(a) and (d) depict the ICA, which encompasses a geared motor equipped with an encoder, input and output couplings, a linear stiffness torsion spring, and micro pulleys interconnected by tendons, all housed within an elongated shell.

The ICA supports both unidirectional and bidirectional contraction modes. In bidirectional mode, tendons (color-coded in red and blue) are affixed to a driven pulley connected to the output coupling. To minimize friction, the left (red) tendon is routed through two pulleys on the left, while the right (blue) tendon traverses internal rails, emerging on the right via three pulleys. In unidirectional mode, only the left tendon is operational.

The ICA’s elastic component integrates a torsion spring, flanked by input and output couplings. The motor’s output shaft hosts the input coupling. The torsion spring introduces a decoupling between these couplings, ensuring that any resistance experienced by the tendon amplifies the angular disparity between the couplings, causing the torsion spring to deform. This deformation facilitates energy absorption and eventual reversion to the original state, granting the desired compliance.

The ICA presents multiple merits. Notably, its reduced outer diameter facilitates the selection of a torsion spring harmonized with the motor’s diameter, ensuring protection without necessitating increase in actuator diameter. Furthermore, by leveraging active tendons at both extremities, the ICA can achieve double the output speed compared to single-ended actuators of a similar motor and driving pulley composition.

Nonetheless, challenges persist. The motor’s diameter inherently delimits the dimensions of the feasible torsion spring, imposing restrictions on the attainable elasticity coefficient and peak torque. Such constraints may potentially result in

a limited rated torque for the chosen motor. Opting for a diminished elasticity coefficient might cause the torsion spring to surpass its maximal deformation threshold before the motor reaches its rated torque, jeopardizing the actuator's intrinsic 'soft' characteristic.

3.2 External Spring Compliant Actuator (ECA)

To address the ICA's constraints concerning output force, the second actuator, ECA, prioritizes enhancing the elastic force. By increasing the actuator's outer diameter and incorporating a high stiffness compression spring around the motor, the ECA simultaneously achieves a more compact length and superior controllable output force.

Fig. 1(b) and (e) illustrate the ECA's architecture, which encompasses a geared motor (designated as the contractile element), driving and auxiliary pulleys, an enveloping external spring (termed the elastic element), tendons, and a cable connector. The contractile and elastic elements are sequentially linked, encased within a slim shell which is encircled by the external spring.

Contraction is facilitated by attaching one extremity of the left tendon to the driving pulley. This tendon then traverses two pulleys — reducing friction — and is anchored to an external attachment point. Rotation of the motor shaft prompts the driving pulley to contract this tendon.

Unique to the ECA is its compression spring situated externally to the shell. This spring's right extremity is anchored by a tab, with its left counterpart interacting with three tab-fitted sliders. These sliders, which navigate along rails on the shell, modulate the spring's deformation. Three tendons (highlighted in blue) commence within this external spring, each affixed to a slider, and converge at a mobile cable connector, not rigidly attached to the actuator. When tension is exerted on the consolidated tendon, the rightward (blue) tendon activates the cable connector, prompting the sliders and compressing the spring.

In juxtaposition with the ICA, the ECA boasts a reduced length, compensating with a larger outer diameter. This strategic envelopment of the compression spring around the motor capitalizes on the motor's inherent length, enhancing compactness — a crucial feature for applications in space-restricted joints like the deltoid muscles. By permitting a more generous outer diameter, the ECA can adapt to a spectrum of compression springs, varying in elasticity coefficients and compression thresholds, facilitating a substantial controllable output force. The ability to utilize a longer spring, without extending actuator length, offers expansive elastic displacement.

Nonetheless, the ECA's enlarged outer diameter is its conspicuous drawback, potentially resulting in disproportioned limbs. Furthermore, the inherent weight of sizable compression springs might diminish the power density.

4 Modeling and analysis of the actuators

In tendon-driven joints, actuators in an antagonistic pair configuration are used to achieve the desired joint position θ and output torque. The three actuators (ICA, ECA, MISA) presented are appropriate for these robot joints. Fig. 2 illustrates the simplified configuration of the actuation system and its corresponding operation process. The three steps for joint actuation are described. The diagram depicts the elastic elements and tendons as springs for simplification purposes.

4.1 Force and tendon displacement relationship

When the two ends of the tendons are limited, a tendon displacement d_i (the subscript $i = 1, 2$ stands for ICA, ECA, respectively). The same rule is followed for other variables that contain subscript i is generated due to the deformation of the elastic element and tendon when the motor rotates by angle α . Assuming $d_i = d_{mi}$ (the maximum value of d_i , the tendon deformation is included) when the elastic elements reach the limited position while the tension is F_{tmi} .

Before the elastic elements reach the limited position ($0 \leq d_i \leq d_{mi}$), the elastic elements and tendons are deformed. The elastic coefficient of tendon displacement in ICA due to the deformation of the torsion spring is equivalent to $k_{ts} = k_{e2}/2\pi r^2$, where k_{e2} represents the torsion spring's elasticity coefficient and r denotes the radius of the output pulley. In the design of ICA, the tendon passes over three supporting pulleys, leading to a friction force of $F_f = \mu_p F_t$, where μ_p represents the friction coefficient. The stiffness of the elastic element in ECA is denoted as k_{cs} and corresponds to the elasticity coefficient of the compression spring. The friction can be ignored.

The relationship function between F_t and d_i at this stage $F_t = f_d(d_i)$ can be deduced as:

$$d_i = \begin{cases} (F_t - F_f) \frac{1}{k_{ts}} + F_t \frac{1}{k_{ti}} & i = 1 \\ F_t \frac{1}{k_{cs}} + F_t \frac{1}{k_{ti}} & i = 2 \end{cases} \quad (1)$$

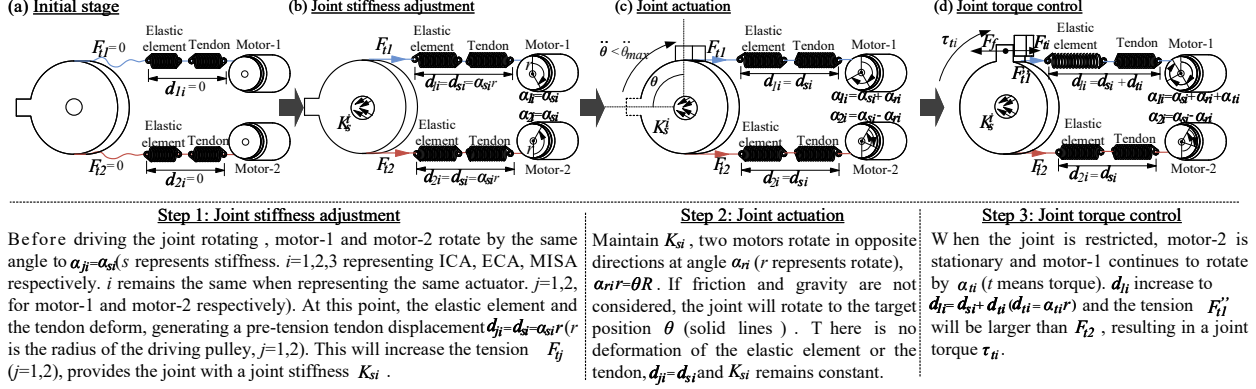


Figure 2: The process of using two compliant actuators to drive the joint movement through tendons. (a) In the initial stage, the tendons in both actuator 1 and 2 are not under tension; (b) applying joint stiffness to the joint by tensioning the tendons; (c) driving the joint to the target angle; (d) controlling the joint torque when the joint is restricted.

Where k_{ti} denotes the elasticity coefficient of the tendon.

After the elastic elements reach the limited position ($d_i > d_{mi}$), F_t will only stretch the tendon. $F_t = f_d(d_i)$ in this stage is:

$$d_i = d_{mi} + (F_t - F_{tmi}) \frac{1}{k_{ti}} \quad (2)$$

By combining the two stages, the relationship between the applied force F_t and the displacement d_i can be expressed as a function:

$$F_t = f_{di}(d_i) \quad (3)$$

4.2 Joint stiffness adjustment

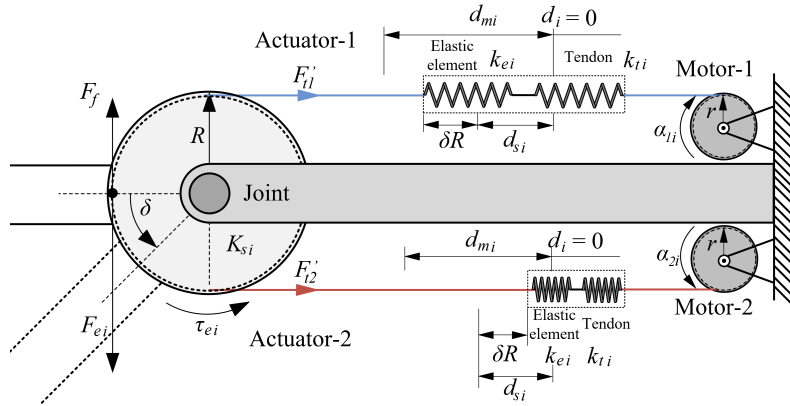


Figure 3: Joint stiffness adjustment using a pair of compliant actuators.

For a comprehensive comparison of ICA, ECA, and MISA, the previously established methodology [28] for joint stiffness application was reiterated. As in step 1 in Fig. 2(b), the motor 1 and 2 rotate simultaneously before actuating the joint rotates, deforming the elastic elements and tendons to produce pre-tension tendon displacement d_{si} ($i = 1, 2$). According to the function (3), the tension on the actuators F_{tj} ($j = 1, 2$ denotes the actuator 1 and actuator 2 respectively). The same rule is followed for other variables that contain subscript j is:

$$F_{tj} = f_{di}(d_{si}) \& (i = 1, 2; j = 1, 2) \quad (4)$$

A joint stiffness K_{si} will be applied to the joint. A small K_{si} may lead the joint to oscillate easily under system vibration and a large K_{si} may result in large joint friction. As shown in Fig. 3, after K_{si} has been loaded, applying a virtual external torque $\tau_{ei} = F_{ei}R$ (F_{ei} denotes the virtual external force, R denotes the joint moment arm) to the

joint will result in a passive rotation angle δ (rotates to the dashed position). K_{si} refers to the level of effort required to produce a passive rotational angle δ with τ_{ei} , which is:

$$K_{si} = \frac{\tau_{ei}}{\delta} = \frac{F_{ei}R}{\delta} \quad (5)$$

As described in Fig. 2(b) and Fig. 3, by applying τ_{ei} , F_{t1} will increase to F'_{t1} while d_{j1} on actuator 1, d_{1i} to $d_{1i} = d_{si} + \delta R$. F_{t2} will decrease to F'_{t2} while d_{2i} to $d_{2i} = d_{si} - \delta R$. F_{ei} can be calculated as:

$$F_{ei} = F'_{t1} - F'_{t2} + F_f \quad (6)$$

Where $F_f = \mu_s F_{tj}$ refers to the static frictional force acting on the joint, μ_s represents the static friction coefficient.

Combined (3) and (6), F_{ei} can be represented as:

$$F_{ei} = f_{di}(d_{si} + \delta R) - f_{di}(d_{si} - \delta R) + \mu_s F_{tj} \quad (7)$$

For different d_{si} , there are five stages when the joint is passively rotated.

The first stage is when $0 \leq d_{si} \leq \delta R$, τ_{ei} causes the elastic element in actuator 2 to resume its initial position. i.e. $F'_{t2} = 0$. According to (7), F_{ei} at this stage is:

$$\begin{bmatrix} F_{e1} \\ F_{e2} \end{bmatrix} = \begin{bmatrix} k_{et1} & 1 + \mu_s \\ k_{et2} & 1 + \mu_s \end{bmatrix} \begin{bmatrix} \delta R \\ F_{tj} \end{bmatrix} \quad (8)$$

Where $k_{et1} = k_{ts}k_{t1}/[k_{t1}(1 - \mu_p) + k_{ts}]$ and $k_{et2} = k_{cs}k_{t2}/(k_{t2} + k_{cs})$ are the stiffness of ICA and ECA during the springs working stage when the deformation of the tendon is considered.

The second stage is when $\delta R < d_{si} \leq d_{mi} - \delta R$, τ_{ei} causes the elastic element in actuator-1 further to deform but yet reach the maximum deformation. In this stage, the elastic element in actuator 2 resumes partial deformation and remains in a partially deformed state, unable to return to its original state. F_{ei} at this stage is:

$$\begin{bmatrix} F_{e1} \\ F_{e2} \end{bmatrix} = \begin{bmatrix} k_{et1} & \mu_s \\ k_{et2} & \mu_s \end{bmatrix} \begin{bmatrix} 2\delta R \\ F_{tj} \end{bmatrix} \quad (9)$$

In the initial two phases, joint stiffness emanates from the deformation of the elastic component. The force-displacement relationship during these stages can be discerned by integrating the relevant parameters into the designated equation. Practically, complete relaxation of the tendon should be avoided to prevent the actuator from dislocation, this also impacts the control precision of the joints. The second stage is the stage in which the joint stiffness can be controlled. The minimum and maximum controllable joint stiffnesses are denoted as K_{smini} , K_{smaxi} with a range denoted as ΔK_{si} . In the following three stages, the deformation of the tendon contributes to the joint stiffness adjustment. The tendon stiffness k_{ti} is assumed to be constant, whereas practically k_{ti} may vary. The following stages are therefore non-controllable joint stiffness stages.

The third stage is when $d_{mi} - \delta R < d_{si} \leq d_{mi}$, the elastic element in actuator 1 is fully deformed to the limited position, the tendon is stretched further. The elastic element of the actuator 2 resumes partial deformation. F_{ei} at this stage is:

$$\begin{bmatrix} F_{e1} \\ F_{e2} \end{bmatrix} = \begin{bmatrix} F_{tm1} & \mu_s - 1 & k_1 \\ F_{tm2} & \mu_s - 1 & k_2 \end{bmatrix} \begin{bmatrix} 1 \\ F_{tj} \\ \delta R \end{bmatrix} + \begin{bmatrix} F_{k13} \\ F_{k23} \end{bmatrix} \quad (10)$$

Where $k_1 = k_{et1} + k_{t1}$, $k_2 = k_{et2} + k_{t2}$, $F_{k13} = k_{t1}(d_{s1} - d_{max1})$, $F_{k23} = k_{t2}(d_{s2} - d_{max2})$.

The fourth stage is when $d_{mi} < d_{si} \leq d_{mi} + \delta r$, the elastic element is in the limited position before τ_{ei} applied. τ_{ei} further stretch the tendon in actuator 1. The tendon in actuator 2 recovery from stretching and the elastic element resumes partial deformation. F_{ei} at this stage is:

$$\begin{bmatrix} F_{e1} \\ F_{e2} \end{bmatrix} = \begin{bmatrix} -F_{tm1} & 1 + \mu_s & k_{t1} \\ -F_{tm2} & 1 + \mu_s & k_{t2} \end{bmatrix} \begin{bmatrix} 1 \\ F_{tj} \\ \delta R \end{bmatrix} + \begin{bmatrix} F_{k14} \\ F_{k24} \end{bmatrix} \quad (11)$$

Where $F_{k14} = (\delta R - d_{s1} + d_{max1})k_{et1}\delta R$, $F_{k24} = (\delta R - d_{s2} + d_{max2})k_{et2}\delta R$.

For the last stage, when $d_{si} > d_{mi} + \delta r$, the elastic element is in the limited position before τ_{ei} is applied. τ_{ei} further stretch the tendon in actuator 1. In actuator 2 the tendon recovers partial deformation. F_{ei} at this stage is:

$$F_{ei} = 2\delta R k_{ti} + \mu_s F_{tj} \quad (12)$$

Combining five stages, F_{ei} can be calculated as a function:

$$F_{ei} = f_{ei}(\delta, d_{si}) \quad (13)$$

Combining (3), (5) and (13), K_{si} loaded to the joints at different d_{si} can be expressed as a function:

$$K_{si} = f_{Ki}(\delta, d_{si}) \quad (14)$$

4.3 Maximum allowable joint acceleration

After joint stiffness K_{si} is determined, the actuators will rotate the joint as the second step in Fig. 2(c). Since the actuators are not fixed, it is critical to prevent the actuators from loosening or even dislocating during joint motion. This subsection calculates the relationship between the maximum allowable angular acceleration $\ddot{\theta}_{max}$ (to avoid tendon slackening) and d_{si} during the joint rotation.

Motor 1 continues to rotate at an angle α_{ri} while motor 2 continues to rotate $-\alpha_{ri}$, where α_{ri} is the driving angle. Assuming the effects of gravity and friction are neglected, the test joint would be actuated to the desired position θ (represented by solid position in Fig. 2(c)) if $\alpha_{ri}r = \theta R$.

During the acceleration of the joint rotation, the joint will be passively rotated by angle δ_r due to the mass moment of inertia. The elastic element in actuator 1 will be further deformed and the tendon displacement will increase to $d_{1i} = d_{si} + \delta_r R$. The elastic element in actuator 2 will partially recover its deformation and d_{2i} will decrease to $d_{2i} = d_{si} - \delta_r R$. If the joint angular acceleration $\ddot{\theta}$ exceeds the allowable maximum value, the elastic element of actuator 2 will restore to its initial position and the tendon will no longer be tensioned ($F_{t2} = 0$). At this point the tendon displacement on actuator 2, d_{2i} will decrease from d_{si} to 0, therefore:

$$d_{si} - \delta_r R = 0 \quad (15)$$

According to (13), the virtual external torque required to passively rotate the joint at angle δ_r is:

$$\tau_{ei} = F_{ei}R = f_{ei}(\delta_r, d_{si})R \quad (16)$$

In order to avoid the tendon slack on actuator 2, τ_{ei} is related to the maximum allowable angular acceleration $\ddot{\theta}_{max}$ as:

$$\tau_{ei} = I\ddot{\theta}_{max} \quad (17)$$

Where I is the rotational inertia of the joint.

$\ddot{\theta}_{max}$ is related to d_{si} . Combining (15), (16) and (17), the relationship can be obtained as:

$$\ddot{\theta}_{max} = \frac{f_{ei}(d_{si}/R, d_{si})R}{I} \quad (18)$$

Here we only consider the situation where the actuator is in the stage when the elastic element operates, so that $d_{si} \leq d_{mi}$.

4.4 Joint torque control

Figure 2(d) illustrates a joint that is restricted and K_{si} is maintained. In this setup, while motor 1 keeps rotating by an angle α_r , motor 2 remains stationary. This causes d_{1i} to increase by d_{ti} , such that $d_{1i} = d_{si} + d_{ti}$, where d_{ti} represents the torque displacement, which is equal to $\alpha_r r$. The force on actuator 2 remains constant at F_{t2} , while F_{t1} increases to F_{t1}' . Using equation (3), we can deduce the tension difference between the two actuators F_{ti} as:

$$F_{ti} = f_{di}(d_{si} + d_{ti}) - f_{di}(d_{si} - d_{ti}) - F_f \quad (19)$$

Thus, the joint should output torque $\tau_{ti} = F_{ti}R$, which is a function of d_{ti} and d_{si} :

$$\tau_{ti} = f_{tdi}(d_{si}, d_{ti}) \quad (20)$$

When $d_{si} + d_{ti} \leq d_{mi}$, where the elastic elements are in the working stage, it is considered as the torque controllable stage. During this stage, the maximum joint torque τ_{tmi} is related to d_{si} :

$$\tau_{tmi} = f_{tdi}(d_{si}, d_{mi} - d_{si}) \quad (21)$$

The above is to output τ_{ti} while maintaining K_{si} , i.e. actuator 2 remains stationary and actuator 1 is in operation. It is also possible to produce a larger τ_{ti} by increasing d_{1i} and decreasing d_{2i} simultaneously when the joint is restricted. At this point, τ_{tmi} will be constant, independent from d_{si} (friction is not considered). If only consider the stages when elastic elements are involved, τ_{tmi} occurs when $F_{t1} = F_{tmi}$ and $F_{t2} = 0$ as:

$$\tau_{tmi} = RF_{tmi} \quad (22)$$

5 Prototypes and comparisons

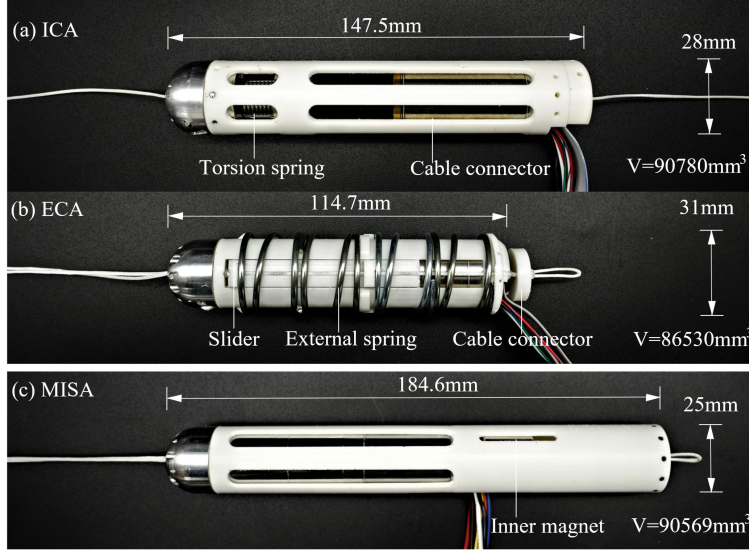


Figure 4: The prototypes of the three compliant actuators: (a) ICA; (b) ECA; (c) MISA [28].

To enable a clear comparison, the ICA, ECA and the previously introduced MISA [28] were developed utilizing identical motors: Maxon brushless motors ECX TORQUE 22 M (24V, 30/43W) with GPX 22 mm 62:1 planetary gearbox. An output pulley with a radius of $r = 5\text{mm}$ is incorporated in each design. The prototypes are depicted in Figure 4, while their key parameters are tabulated in Table 1. Despite varying in diameter and length, the volumes of the three actuators are relatively similar.

Table 1: Performance of the prototypes

	ECA	ICA	MISA
Rated force (N)	250	125	250
Rated speed (mm/s)	110	220	110
Diameter (mm)	31	28	25
Length (mm)	114.7	147.5	184.6
Mass (g)	295	280	335
Volume (mm^3)	86530	90780	90569

Both actuators use the same tendon, which is a braided fishing line with an outer diameter of 1.0 mm and a maximum force of 90.72 kg. The tendon's spring constant k_t was determined to be 30 N/mm through experimentation, and its length is fixed at 200 mm. However, the number of tendons used in each actuator differs, resulting in different values of k_{ti} .

Based on Table 1, ICA is designed to withstand a rated force of 125 N and an ultimate motor torque of 1.25 Nm. However, as a result of the limitations imposed by size, a torsion spring (elasticity coefficient: $k_{e1} = 508 \text{ Nmm/rad}$, maximum deformation: 1 rad) was selected. This corresponds to an equivalent elasticity coefficient of $k_{ts} = k_{e1}/2\pi r^2 = 3.236 \text{ N/mm}$ due to the tendon displacement. The torsion spring reaches the maximum deformation when $F_{tm1} = 112.4 \text{ N}$. Since minimizing the actuator diameter require narrow access inside the shell, the tendons use a single strand of fishing line with $k_{t1} = 30 \text{ N/mm}$ and $d_{m1} = 34.8 \text{ mm}$.

ECA is designed to withstand a rated force of 250 N. A compression spring with an elasticity coefficient of $k_{e2} = k_{cs} = 10.44 \text{ mm/N}$ and a maximum compression of 24.34 mm is selected. The spring is compressed to the solid position when $F_{tm2} = 254 \text{ N}$, providing protection even if the motor reaches the rated torque. The tendon in ECA consists of two strands, and the elasticity coefficient is $k_{t2} = 60 \text{ N/mm}$, resulting in $d_{m2} = 28.5 \text{ mm}$.

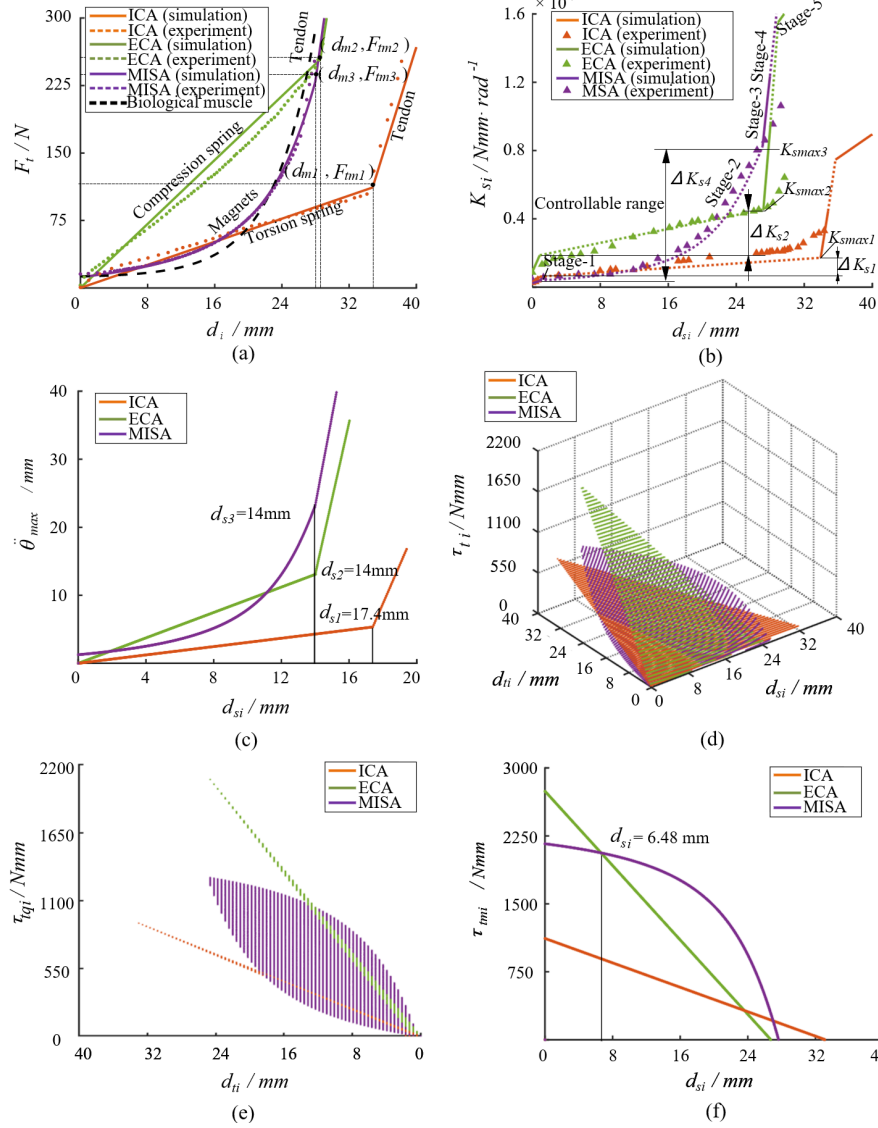


Figure 5: (a) The simulation and experimental results of the three compliant actuators, $F_t = f_{di}(d_i)$, and the tension-length curve of the biological muscle; (b) $K_{si} = f_{Ki}(\delta = 0.087, d_{si})$; (c) Simulation result of the relation between $\dot{\theta}_{max}$ and d_{si} ; (d) $\tau_{ti} = f_{tdi}(d_{si}, d_{ti})$ ($R = 10$ mm); (e) side view of $\tau_{tqi} = f_{tdi}(d_{si}, d_{ti})$ ($R = 10$ mm); (f) relationship between τ_{tmi} and d_{si} .

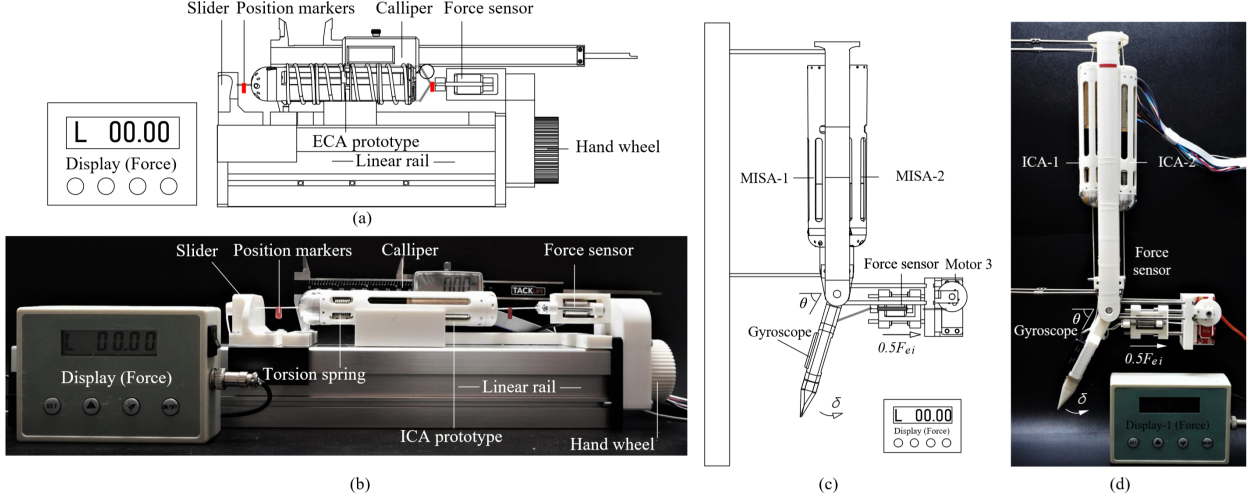


Figure 6: (a) The schematic diagram of the force-displacement relationship test rig. (b) Test rig setup for force-displacement relationship test; (c) The schematic diagram of the variable joint stiffness test rig. (d) Test rig set-up for the adjustable joint stiffness test.

Table 2: Parameters of the prototypes

	ECA	ICA
k_{ei} (N/mm)	$k_{cs} = 10.4$	$k_{ts} = 3.2$
F_{tmi} (N)	252.9	112.4
d_{mi} (mm)	28.5	34.8
k_{ti} (N/mm)	60	30
K_{smini}^1 (Nm/rad)	1.82	0.60
K_{smaxi}^1 (Nm/rad)	3.12	1.15
ΔK_{si}^1 (Nm/rad)	1.30	0.52
τ_{tmi}^2 (Nm)	2.77	1.12

¹ $\delta = 0.087$ rad, $\mu_e = 0.1$, $\mu_s = 0.1$, $r = 5$ mm, $R = 10$ mm.

² τ_{tmi} is calculated while Motor-2 remains stationary.

5.1 Comparison of simulation results

In this subsection, the simulation results of the ICA, ECA and MISA [28] will be presented and compared. ICA is represented in orange, ECA in green and MISA in purple.

The parameters of the actuators are presented in Table 2. Fig. 5(a) displays the simulated force-displacement relation, $F_t = f_{di}(d_i)$. The curve for the biological muscle is represented by the dashed blue line in Fig. 5(a), indicating a rise in stiffness as displacement increases. For acquisition details, refer to our previous work [28]. This non-linear behaviour can provide quick protection against unexpected impacts. MISA aims to replicate the non-linear stiffness exhibited by biological muscles. By comparing the solid and dashed blue curve in Fig. 5(a), it is demonstrated that the trends in MISA closely coincide with that of biological muscle. In contrast, the force-displacement relations for the ICA and ECA are linear.

A pair of ICAs, ECAs and MISAs were applied to the same test joint ($R = 10$ mm) respectively. By adjusting d_{si} , according to (14), different joint stiffness K_{si} can be provided to the joint. K_{si} is related to δ and d_{si} . In Fig. 5(b), the relationship between K_{si} and d_{si} when $\delta = 0.087$ rad is illustrated, i.e. $K_{si} = f_{Ki}(\delta = 0.087, d_{si})$. As described in the previous section, five stages of K_{si} are distinguished by different line types. The second stage, which is the controllable joint stiffness stage, is indicated by the dotted lines in Fig. 5(c).

According to Fig. 5(a), ECA and MISA share similar F_{tmi} ($F_{tm2} \approx F_{tm3}$). But using the same calculation methodology, it can be observed from Fig. 5(b) that the joint using MISAs has the ability to realize a board range of joint stiffness compared to ECAs, $\Delta K_{s3} = 7850$ Nmm/rad, 2.9 times the $\Delta K_{s2} = 2640$ Nmm/rad of ECAs. The maximum controllable

joint stiffness achievable with the MISA is $K_{smax3} = 8235$ Nmm/rad, 1.83 times the $K_{smax2} = 4507$ Nmm/rad of the ECA. The minimum controllable joint stiffness for the joint with ECAs is 1867 Nmm/rad, lower joint stiffnesses cannot be achieved.

Fig. 5(c) shows the maximum allowable angular acceleration $\ddot{\theta}_{max}$ during joint rotation with different d_{si} (different K_{si}). $\ddot{\theta}_{max}$ is positively related to d_{si} . A marked escalation is observed in $\ddot{\theta}_{max}$ once d_{si} surpasses a specified threshold. ($d_{s1} > 14$ mm, $d_{s2} > 17.4$ mm, $d_{s3} > 14$ mm). This occurs as the tendon in actuator-1 experiences stretching before the tendon in actuator-2 has fully slackened, a situation that is further compounded by the tendon's high elasticity coefficient.

τ_{ti} , in relation to d_{si} and d_{ti} , $\tau_{ti} = f_{tdi}(d_{si}, d_{ti})$ is shown in Fig. 5(d) and (e). Using this relationship, joint torque control can be achieved. If only consider the elastic element working stage, i.e. $d_{si} + d_{ti} \leq d_{mi}$, the maximum output joint torque τ_{tmi} is only related to d_{si} as shown in Fig. 5(f). It can be seen that τ_{tmi} decreases if d_{si} increases. When $d_{si} < 6.48$ mm, the joint with ECAs is able to output a larger torque than that with MISAs, $\tau_{tm2} < \tau_{tm3}$.

5.2 Verification of Force-Displacement correlation

The test-rig setup is depicted in Fig. 6 (a) and (b), in which the actuator tendon was secured at one end to a force sensor (Dysensor, DYZ-102, 0-500 N), and at the other end was connected to the slider. As the slider was free to move along the linear rail, the position was adjustable using a hand wheel. Position markers were employed to monitor the tendon displacement. The motor was energized during the experiment but remained stationary. The experimental data were recorded by the force sensor and the calliper at various positions of the slider. The associated test videos are provided in the supplemental materials. The obtained results for the actuators are displayed in Fig. 5(a), which are consistent with the simulation results.

5.3 Verification of joint stiffness-displacement relationship

Figs. 6(c) and (d) shows the test set-up for evaluating joint stiffness using a pair of antagonistic actuators applied to a test joint. Motor 3 is responsible for moving the force sensor along a linear rail, which is attached to the driven arm via cables. The movement of the force sensor can rotate the driven arm counterclockwise. The force value is displayed on the display, and a commercialized gyroscope sensor (Brand: Wit-motion, Model: WT901BLECL, Chip: MPU9250) is attached to record the the driven arm's position. The joint stiffness-displacement relation can be tested in the following steps:

Step 1: The joint is driven to the target angle (70°) by the two ICAs without any deformation of the elastic elements.

Step 2: Control Motor 3 rotates and shifts the force sensor gradually towards the right. The external force from the force sensor causes the driven arm to rotate counterclockwise. The force is recorded when the driven arm reaches the desired position (75°). Then control Motor 3 to return to its initial position.

Step 3: Both actuators 1 and 2 are controlled to generate different tendon displacements d_{si} while maintaining the joint position constant at the value achieved in the first step. Then the second step is repeated, and the force readings are recorded throughout the test.

The test results provide the relationship between F_{ei} and d_{si} for each actuator, which in turn determines the relationship between K_{si} and d_{si} . The associated test videos are provided in the supplemental materials. The plot of these results for the three actuators is presented in Fig. 5(b).

6 Application of compliant actuators on the biomimetic robotic arm

The human body and traditional robots differ fundamentally in the type and function of their respective tissues. Traditional robots consist mainly of rigid materials, such as metal and plastic, while the human body is made up of soft tissues, including muscles, tendons, fat, cartilage, and ligaments. This key difference means that the human body possesses unique characteristics such as both tensile and compressive properties, including variable joint stiffness, flexibility, damping, compliance, and more, which are critical for exceptional performance in tasks such as fine motor skills, dexterity, and adaptability to a wide range of environments.

The human musculoskeletal system serves as an ideal model for designing a robotic arm. Fig. 7(a) shows a robotic arm that imitates the skeletal-ligament system of the biological arm, replicating the bones, ligaments, and cartilage of the human arm. For example, the elbow joint is stabilized by ligaments (medial collateral ligament and lateral collateral ligament) instead of being articulated with a shaft. To replicate the medial collateral ligament in the robotic arm prototype, it is divided into three parts: the anterior part (1), middle part (2), and posterior part (3), as shown in

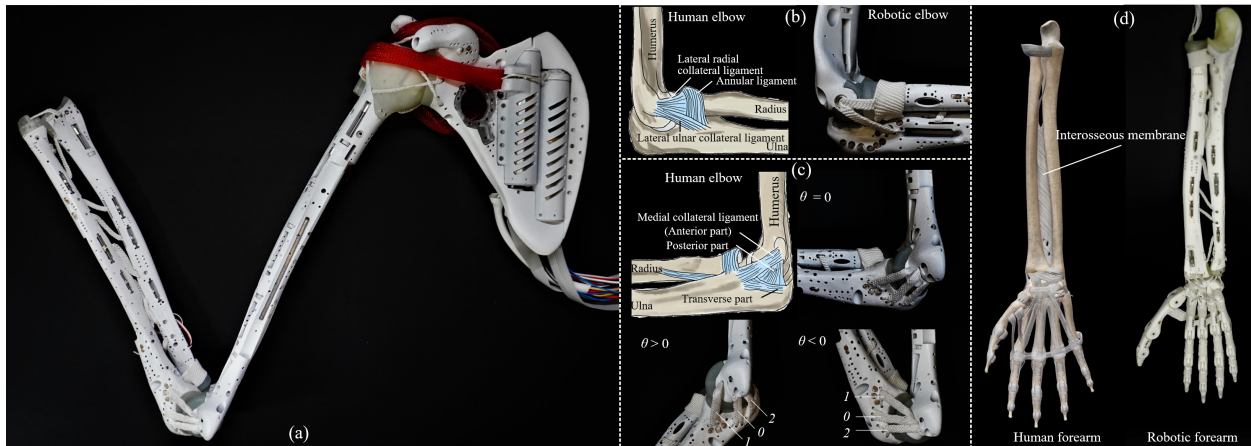


Figure 7: (a) Robotic arm prototype based on human skeleton system. The joint is articulated by ligaments. (b) The lateral collateral ligament and annular ligament of the human elbow and the robotic elbow; (c) Strain varies on each part of the medial collateral ligament when the joint angle changes. Part 1 is under tension when $\theta > 0$, part 2 is under tension when $\theta < 0$; (d) A robotic hand is attached to the arm, a skeletal ligament system similar to that of the human forearm is replicated in the robotic arm.

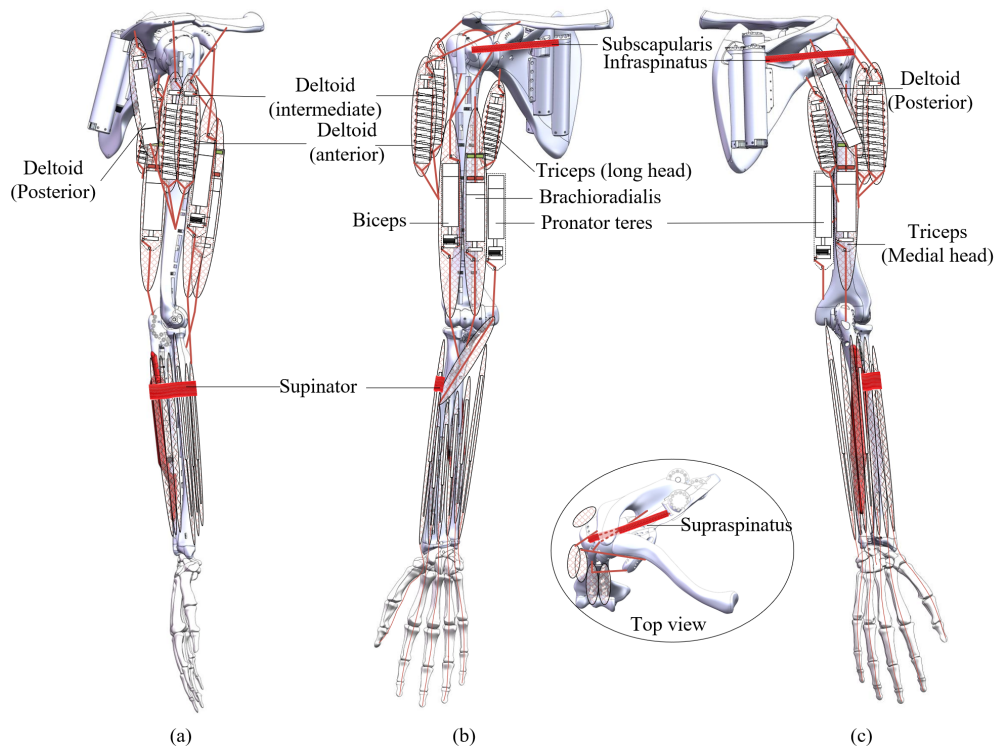


Figure 8: Tendon and muscle arrangement of the proposed robotic arm (right). (a) Right view; (b) Front view; (c) Rear view.

Fig. 7(b). At the initial position ($\theta = 0$), all three parts of the ligament are at their original length. This arrangement allows the middle part (2) to provide stability throughout the rotation of the elbow, while the tension on the posterior part (3) increases sharply as the joint approaches full flexion ($\theta < 0$), preventing joint dislocation. Similarly, as the joint approaches full extension ($\theta > 0$), the tension on the anterior part (1) increases dramatically to limit the range of motion. The annular ligament and lateral collateral ligament are also replicated in the elbow as shown in Fig. 7(c). These ligaments are knitted with high-strength fibre and exhibit spring-like properties, providing biomimetic features to the robotic arm [72]. To reduce friction and provide a joint interface that mimics biology, the elbow contact surface has been coated with artificial cartilage made of durable V2 resin (made by Formlabs, Elongation at break: 55%, Ultimate Tensile strength: 28 MPa, Tensile modulus: 1 GPa). Due to the soft tissues in the elbow, the stiffness and damping of the joint vary during the joint angle change.

The forearm of the human arm is composed of the radius and ulna, which is also the case for the proposed robotic arm. Pronation/supination is achieved by the radius rotating around the ulna. The radius and ulna are articulated by the interosseous membrane, which is also duplicated in the proposed robotic arm, as shown in Fig. 7(d).

The actuators proposed in this paper have been developed primarily for tendon-driven robotic arms featuring highly biomimetic. The robotic arm presented serves as the target robot, which not only demands an appearance that resembles the human body but also a design that adheres to the underlying principles of the human body.

The robotic arm is developed by incorporating nine compliant actuators, as depicted in Fig. 8. Two MISAs work as the brachioradialis and medial head of the triceps. Two ICAs function as the pronator teres and supinator, while an ECA works as the biceps to assist in forearm rotation (the biceps could also assist with elbow actuation). Additionally, another ECA serves as the long head of the triceps for shoulder adduction and three ECAs work as the Deltoid. 12 major muscles are applied to the robotic arm, as listed in Table 3. The actuators responsible for driving the subscapularis, infraspinatus, supraspinatus, wrist flexor/extensor, and abductor/adductor, are not designed as compliant actuators. The robotic arm prototype is shown in Fig. 9.

Table 3: Artificial muscles applied in the proposed robotic arm.

Joint	Muscle	Type
Shoulder	Deltoid (anterior)	ECA
	Deltoid (intermediate)	ECA
	Deltoid (posterior)	ECA
	Subscapularis	Without compliance
	Infraspinatus	Without compliance
	Supraspinatus	Without compliance
	Triceps (Long head)	ECA
Elbow and forearm	Biceps	ECA
	Brachioradialis	MISA
	Triceps (Medial head)	MISA
	Pronator teres	ICA
	Supinator	ICA
Wrist	Wrist flexor/extensor	Without compliance
	Wrist abductor/adductor	Without compliance

6.1 Exploring joint flexibility and workspace efficiency

The elbow, forearm, wrist, and glenohumeral joint are designed with few joints to achieve multiple degrees of freedom and a large range of motion, reflecting the compactness of the human upper limb. Given the irregular geometrical nature of the joint surfaces, deriving the joint motion angles via simulation proves challenging. Consequently, an experimental approach was employed to ascertain the range of motion for each joint. To record each active joint motion, the scapula of the robotic arm is fixed to the platform, and a gyroscope is used. Before each experiment, the gyroscope is calibrated, and its position is modified so that each measured joint motion corresponds to a change in the x-axis rotation angle. The test results are shown in Fig. 10 and Fig. 11, and the recorded ranges are compared with the data for the human arm, which is presented in Table. 4.

The observed limitations within the prototype pertain to the omission of pectoralis major and latissimus dorsi, restricting the glenohumeral joint's flexion and extension range. Moreover, actuator positioning around the forearm for finger and wrist actuation slightly impedes forearm pronation. Significantly, the prototype's stationary scapula curtails shoulder complex abduction/adduction, mirroring a substantial reduction compared to human arm mobility. This fixed

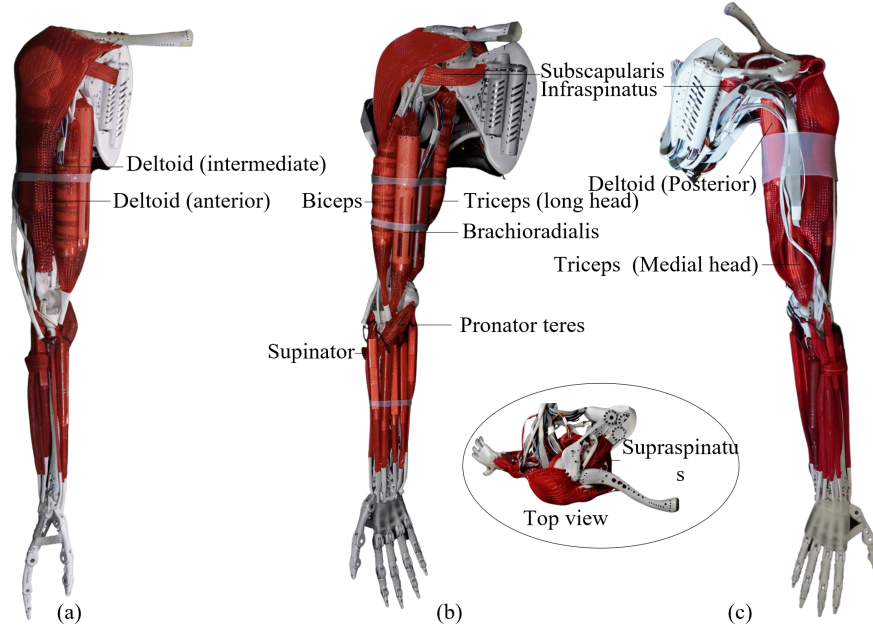


Figure 9: The proposed robotic arm. (a) Right view; (b) Front view; (c) Rear view.

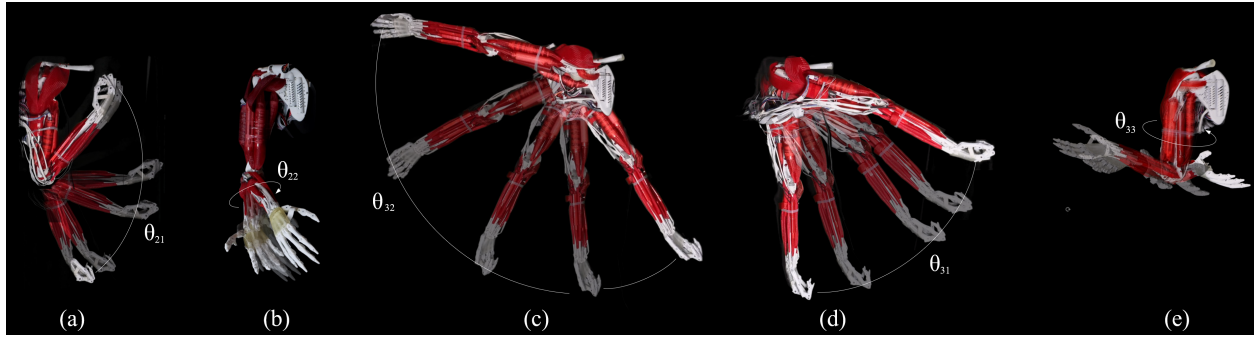


Figure 10: Range of motion test for each motion in the proposed robotic arm. (a) Elbow flexion/extension; (b) Forearm rotation; (c)Glenohumeral joint adduction/abduction; (d) Glenohumeral joint flexion; (e) Glenohumeral joint rotation.

scapula position further hinders rearward extension of the glenohumeral joint, collectively delineating the prototype’s biomechanical divergences and underscoring the necessity for refined actuator and musculoskeletal design to better emulate human motion intricacies.

The kinematic model of the robotic arm is presented in Fig. 12, which comprises 7 revolute joints. As the scapula motion in the shoulder complex was not considered in the early prototype, the first three joints account for the motion

Table 4: The joint range of motion of the robotic arm and human arm (data from [73], [17]).

Motion group	Symbols	Joint range of motion (robotic arm)	human arm
Glenohumeral extension (-) / flexion (+)	θ_{31}	-40*-65°	-60°-167°
Glenohumeral adduction (-) / abduction (+)	θ_{32}	-32°-104°	-29°-100°
Glenohumeral internal (-) / external (+) rotation	θ_{33}	-90°-40°	-97°-34°
Elbow extension (-) / flexion (+)	θ_{21}	0-138°	0-146°
Forearm pronation (-) / supination (+)	θ_{22}	-60°-65°	-70°-70°

*The position of the glenohumeral joint extension was measured in the skeletal system.

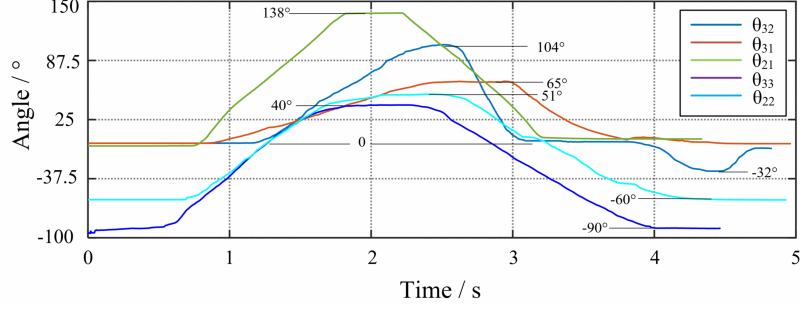


Figure 11: Data recorded of the range of motion test.

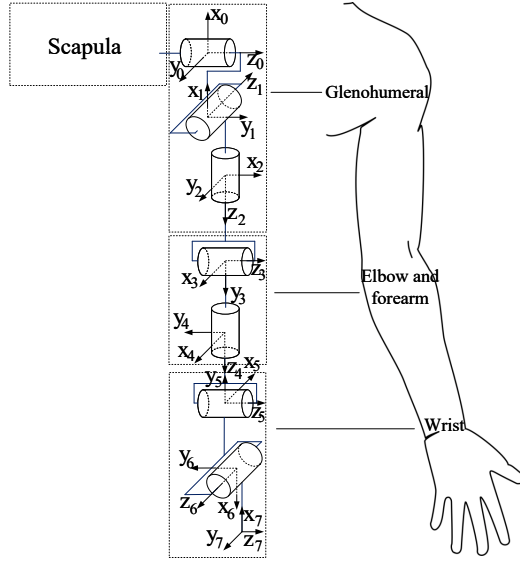


Figure 12: The kinematic model of the proposed robotic arm (the hand is not included).

of the glenohumeral joint, which is well-modelled as a ball-and-socket joint. The fourth joint represents the elbow, while the fifth joint is for forearm rotation. The last two joints contribute to a 2-DOF wrist. Although there is a slight misalignment between the axis of forearm rotation and the wrist motion, this is disregarded in this model. According to the Denavit-Hartenberg convention, coordinate frames are attached to the joints as shown in Fig. 12, and the D-H parameters of the kinematic chain are presented in Table 5.

Table 5: Denavit-Hartenberg parameters of the kinematic model.

axis, i	a_i	d_i	α_i	θ_i
1	0	0	$\pi/2$	θ_{31}
2	0	0	$-\pi/2$	$\pi/2 - \theta_{32}$
3	0	b	$\pi/2$	$\pi/2 + \theta_{33}$
4	0	0	$-\pi/2$	θ_{21}
5	0	c	$-\pi/2$	$\pi + \theta_{22}$
6	0	0	$-\pi/2$	$-\pi/2 - \theta_{11}$
7	0	d	$\pi/2$	θ_{12}

The range of motion for each joint is utilized to determine the workspace, or the reachable area of the robotic hand, as depicted in Fig. 13. This workspace closely mirrors that of the human arm (scapula motion is not considered) when maintaining the same limb length.

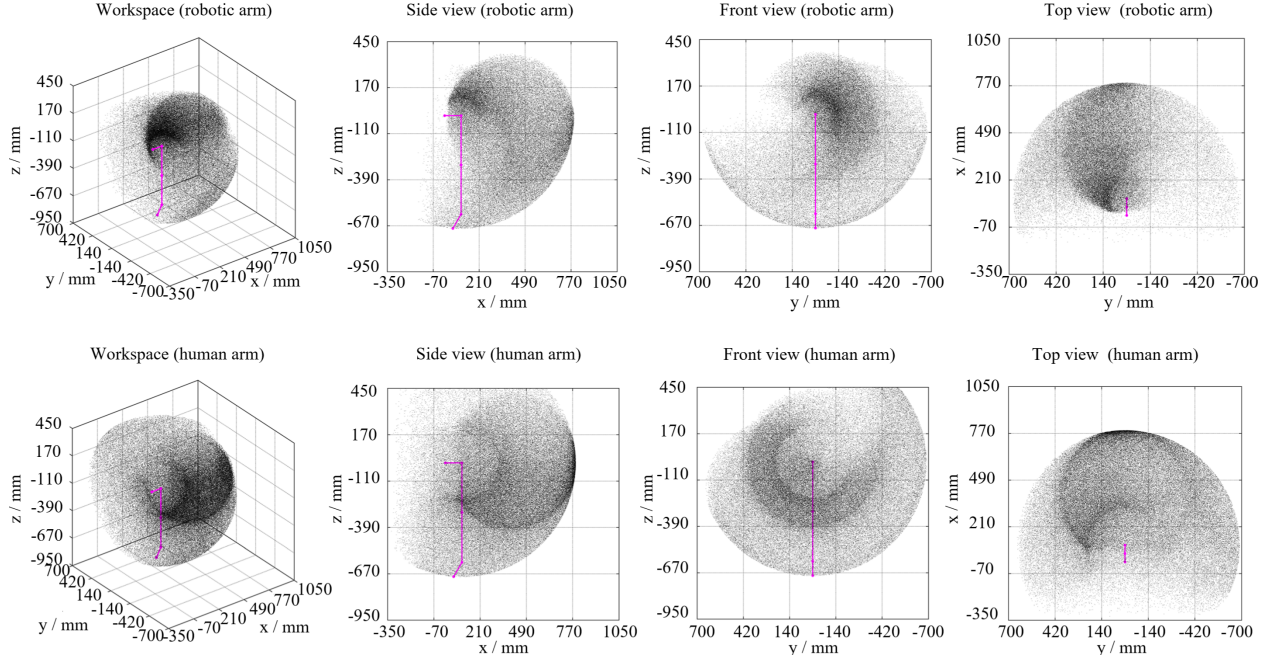


Figure 13: The workspace of the hand in the proposed robotic arm and human arm(Monte Carlo method is applied)

6.2 Performance evaluation of the robotic arm powered by the compliant actuators.

Owing to the high performance of the compliant actuators, the robotic arm exhibits versatility across various environments, despite its dimensions being constrained to human-arm proportions. This robotic arm can be used in a variety of scenarios, such as playing table tennis or badminton which require high end-effector speed, or handling heavy objects which demand high load capacity.

Achieving high speed in industrial robotic arms is relatively straightforward and can typically be accomplished by incorporating appropriate motors and reducers based on design specifications. However, in the development of highly biomimetic robotic arms, stringent restrictions on size and form factor severely limit the available choices for drive mechanisms. Consequently, finding a solution ensuring ample output torque while achieving high-speed operation at the end-effector poses a substantial challenge. One example of a high-speed manipulator is the WAM Arm from Barret Technology, which weighs 27 kg and has a maximum end-effector speed of 3 m/s according to its official specifications [74]. To test the performance of the compliant actuators in driving a robotic arm to output high speed, a table tennis-playing scenario was used. The arm was controlled so that the elbow and shoulder joints flexed simultaneously to hit the ping pong ball before returning to the initial position, as shown in Fig. 14. The test was conducted with a low load on the compliant actuators (the ping pong paddle weighed 238 g, forearm weighed 1 kg, the whole arm weighted 4 kg), and the actuators could operate at their maximum speed (110 mm/s). The instantaneous speed of the end-effector reached 3.2 m/s, and the time taken from the start of the arm flexion to hitting the ping-pong ball was 188 ms.

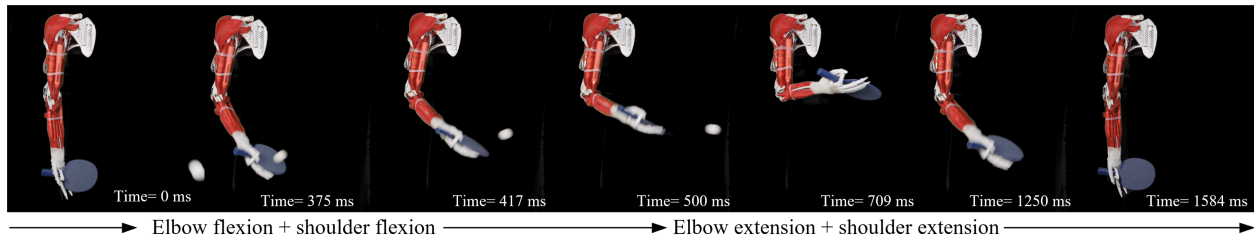


Figure 14: Table tennis playing test.

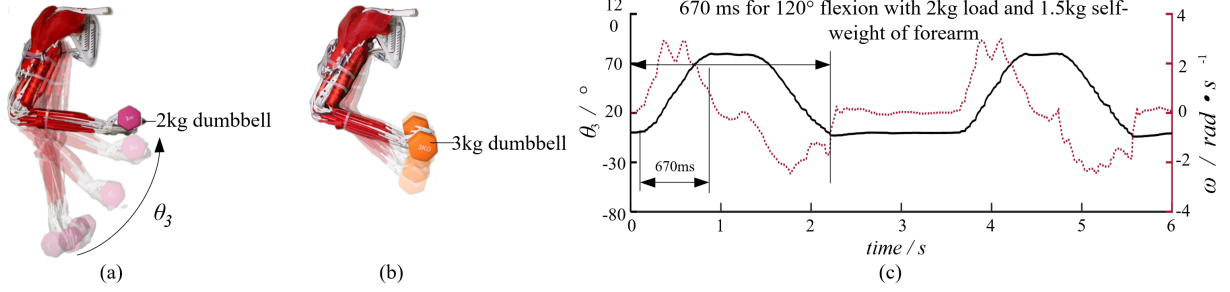


Figure 15: A dumbbell lifting test. (a) Test with 2kg dumbbell; (b) Test with 3kg dumbbell; (c) The forearm position θ_2 and the angular velocity ω recorded at the maximum achievable speed as well as acceleration that did not overload the actuators.

To demonstrate that the robotic arm with the proposed compliant actuators is capable of outputting a large payload at a fast speed, it imitates the human arm lifting dumbbells. The forearm's position was recorded using a gyroscope. In this bionic arm, elbow flexion can be driven by both the brachialis (MISA) and biceps (ECA).

The biomimetic robotic arm's performance was tested by holding a dumbbell (2 kg) with the elbow flexed to 120° and then extended, as shown in Fig. 15(d). Two MISAs were used, and the motor was equipped with a safety mechanism that cuts off excessive speed or abrupt acceleration. The associated test videos are provided in the supplemental materials. The forearm's position θ_2 and angular velocity ω were recorded, as shown in Fig. 15(e), with the maximum permitted speed and acceleration. The test results showed that the elbow fully flexed and lifted the 2 kg weight in 0.67 s, achieving over 0.74 Hz of maximum speed (excluding intervals in full flexion). At $\theta_3 = 50^\circ$ and $\omega = 3$ rad/s, the maximum joint torque, including gravity resistance, surpassed 12 Nm, with the peak power registering at 36 W.

To validate the applicability of MISAs and ECAs to highly biomimetic robotic arms in performing high-intensity tasks, lifting tests were conducted with the robotic arm holding a 3kg dumbbell while both actuators worked simultaneously, as shown in Fig. 15(c). However, the actuator's moment arm driving the joint is shorter when the elbow joint angle is either smaller, nearing full extension, or larger, approaching full flexion. In such cases, lifting a dumbbell necessitates a greater tension output from the actuator on the tendon. This phenomenon is mirrored in the human arm as well. To avert potential damage to the prototype, tests were deliberately not conducted at points of full extension and flexion of the elbow. During the test, the peak joint output torque exceeded 16 Nm, taking into account the resistance of gravity, at lower joint speeds.



Figure 16: Door open test of a biomimetic robotic arm.

Fig. 16 shows the robotic arm is applied to the door opening task. In the test, the robotic hand is first actuated to hold the door handle by driving the ICA-1 to assist in forearm rotation. The long head of the triceps (ECA-1) then drives the shoulder adducted and turns the door handle to unlock the door. Next, the elbow was flexed by two MISAs and pulled the door. Then the elbow is extended and pushed the door back. The associated test videos are provided in the supplemental materials. Experimentally, a torque exceeding 1.5 Nm was required to unlock the door handle. This test may verify that the robotic arms with proposed compliant actuators can be used in challenging daily tasks.

The list of videos for testing the proposed actuators and demonstrating the capabilities of the robotic arm are provided in Table 6. The supplementary video is accessible via the following link: <https://youtu.be/uunLkb-wOK0>.

7 Discussions

The results of the table tennis playing and dumbbell lifting tests provided evidence of the high power output of MISAs, despite their small size and weight. The door opening test confirms the versatility of the proposed three actuators

Table 6: Multimedia extensions are accessible via the link: <https://youtu.be/uunLkb-w0K0>

No.	Description
Video 1	Force-displacement relationship test
Video 2	Experimental of joint stiffness adjustment by applying two MISAs
Video 3	Accomplishment of variable joint stiffness with MISAs - passive mode
Video 4	Accomplishment of variable joint stiffness with MISAs - active mod
Video 5	Passive performance of the robotic arm by applying compliant actuators
Video 6	Table tennis playing test
Video 7	Dumbbell lifting test (2kg and 3kg)
Video 8	Door open test

and their ability to work together seamlessly to execute complex actions. The successful completion of these tasks underscores the potential of highly biomimetic robotic arms equipped with MISAs, ICAs, and ECAs to perform challenging tasks with high-intensity demands without sacrificing the natural appearance of human-like robots. Overall, these experiments demonstrate the great potential of proposed actuators in enabling highly functional and aesthetically pleasing robots that can perform a wide range of tasks with exceptional power.

These three motor-based artificial muscles are intended for highly biomimetic robotic arms. This is a new direction in robotics design: all robot joints without rigid shafts, using ligaments to stabilise the joints; driven by muscles that are not mechanically fixed and have similar human arm muscle arrangement, imitating the actuation method used in human joints; a skeletal model of the human arm is used directly as the main structure of the robot. Unlike conventional robotic arms where the joints are driven directly by motors, the actuators of the biomimetic robotic arm are placed parallel to the skeleton, achieving compactness with high space utilisation and allowing the use of high-power actuators. From the simulations and experimental results, it was preliminarily evidenced that MISA had the highest performance. The advantage of MISA, which was described in [28], enables a wide range of joint stiffness, and achieves a high power-to-volume ratio ($345 \times 10^3 \text{ W/m}^3$). But each of the three actuators had irreplaceable advantages and was therefore applied to the robotic arm prototype.

For the ICA, the unique advantage is that it can be applied in both remote and local tendon-driven methods. When the ICA works in unidirectional output mode, the actuator can be mechanically fixed and the contracted tendon can drive the joint remotely. Both ECA and MISA can only be used in local tendon-driven, where two tendons are connected to the driving arm and driven arm respectively. MISA and ECA require axial movement and sufficient installation space. In the development of the robotic arm prototype, a 22 mm diameter motor was used to achieve a large torque of forearm pronation. Due to limited installation space, implementing MISA or ECA at the location of the pronator teres proves to be impractical with the local tendon-driven approach. Thus, the ICA was mechanically fixed to the humerus to drive the forearm pronation with the remote tendon-driven method.

The first unique advantage of the ECA is its short length. The total actuator length is only 7.2% longer compared to the motor, whereas it is 35.8% for the ICA and 59.1% for the MISA. The second unique advantage is the selection of springs that allow for a high coefficient of elasticity. High-torque motors can be used to achieve large tendon output forces. For the MISA, the maximum repulsive force between the magnets limits the maximum tendon output force (excessive force would disable the protection, and large repulsive force requires oversized magnets). As for the ECA, it allows for a large spring outer diameter with a large maximum compression force, and a large maximum tendon output force can be achieved. In the robotic arm prototype, the elbow joint is driven by the brachialis, biceps, and triceps. The brachialis and triceps can be antagonistically arranged (both connected to the ulna) using a pair of MISAs, which allows variable joint stiffness. The biceps have no antagonistic muscles attached to the radius in the robotic arm prototype, so even if the MISA is used as the biceps, the variable stiffness function of the humeroradial joint will not be realized. The MISA is not considered to function as the biceps muscle. In addition to actuating the forearm supination, the biceps also assist in driving the elbow joint flexion, so that the large tendon output force can significantly increase the joint output torque. Based on the considerations listed above, the ECA was used to simulate the biceps by combining the drawbacks of the MISA with the two unique advantages of the ECA.

For the Deltoid muscles, ensuring robust output force is pivotal for delivering adequate torque to the shoulder joint. An inadequately elastic spring risks reaching its solid state even under no load, rendering the elastic component of the actuator ineffective upon load application. Among various actuators evaluated, only the ECA can be adapted with a high-stiffness elastic element and possesses a straightforward adjustment for peak output force. Consequently, the ECA, equipped with a higher stiffness spring, was selected as the actuator for the deltoid. As illustrated in Fig. 17(a), this ECA features a compression spring with a stiffness of 14.5N/mm and a peak elastic force of 622.7N, making it suitable as a Deltoid actuator. This configuration, when compared to the ECA with a lower stiffness spring depicted in Fig.

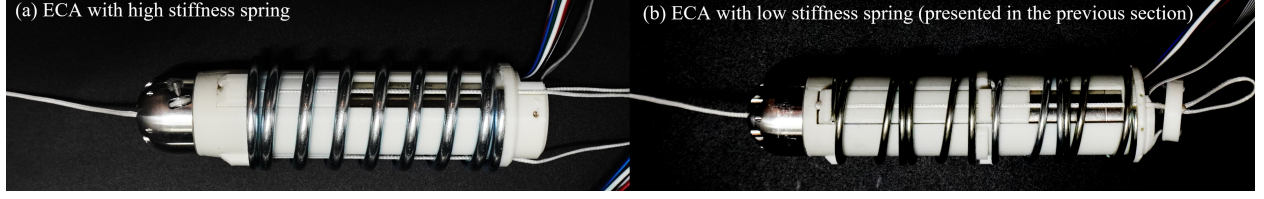


Figure 17: (a) ECA with high stiffness spring; (b) Previous discussed ECA.

17(b) from prior analyses, has a larger diameter and increased weight. However, its elastic force and output forces are augmented by 2.5 times due to the incorporation of a more potent motor (Maxon EC-4 pole, 22mm, 90 W).

The comparison of different compact SEAs is shown in Table 7. In the ECA design (previously analysed), the spring is sleeved over the motor. This design maximises space utilisation and therefore has a significantly higher power-to-volume ratio, which is $361 \times 10^3 \text{ W/m}^3$. the ICA uses a lighter torsion spring and therefore has a higher power-to-mass ratio than the SEAs including the ECA, which is 111.6 W/kg.

Table 7: Comparison of different compact SEAs

SEA	Type ^A	Output ^B (Nm or N)	Elastic ^C (mm or °)	Power (W)	Weight (kg)	Volume ($\times 10^{-6} \text{ m}^3$)	Power/Volume ($\times 10^3 \text{ W/m}^3$)	Power/Mass (W/kg)	Bio ^D
UT-SEA [75]	Linear	848 N	60mm	110	1.168	/	/	94	No
SAFFiR [76]	Linear	300 N	110mm	<80 ^E	0.816	/	/	<98	No
THOR [77]	Linear	600 N	85mm	<80 ^E	0.938	/	/	<85	No
SEA [78]	Linear	136 N	/	44.76	0.4536	333	134	98.7	No
cRSEA [79]	Rotary	10 Nm	$\pm 50^\circ$	<135 ^E	/	/	/	/	No
SEA [80]	Rotary	10 Nm	$\pm 6^\circ$	<65 ^E	1.8	1865	34.85	<36.1	Yes
HT-SEA [81]	Tendon-R	0.3 Nm	/	13.86 ^D	0.393 ^F	100.131 ^F	<138	<35.26	Yes
LC-SEA [82]	Tendon-R	0.5 Nm	/	13.86 ^D	0.383 ^F	92.403 ^F	<149	<36.03	Yes
ICA (proposed)	Tendon-L	125 N	34.8 mm	31.248	0.28	90.78	344	111.6	Yes
ECA (proposed)	Tendon-L	250 N	28.5 mm	31.248	0.295	86.53	361	105.9	Yes

^A The tendon-driven features two modes: R (remote-control) and L (local-control). ^B Maximum output torque or force. ^C Range of passive stroke or passive angular deflection. ^D Whether can be applied to highly biomimetic robotics. ^E Not given in the literature, estimated according to the power of the motor used. ^F The data given in the literature are excluding the motor, they are the estimated value by adding the motor's weight or volume.

8 Conclusion

This paper delineates the design and assessment of two novel compliant actuators, the Internal Torsion Spring Compliant Actuator (ICA) and the External Spring Compliant Actuator (ECA), in juxtaposition with the formerly introduced Magnet Integrated Soft Actuator (MISA). The actuation mechanisms were elucidated, prototypes contrived, and their performance meticulously evaluated. All three actuators manifest aptitude for human-robot interaction and highly biomimetic robot applications, showcasing versatility across various robotic joint configurations without necessitating modifications. This facilitates enhanced naturalism and power output in compact limb designs as opposed to the conventional direct joint-motor shaft linkage. The localized placement of these proposed actuators near the joints augments their functional resemblance to artificial muscles, marking an advancement over existing tendon-driven SEAs.

ICAs are particularly suited for joints with spatial constraints yet demanding high-speed functionality, exhibiting a notable power-to-mass ratio of 111.6 W/kg. On the other hand, ECAs are conducive for joints necessitating substantial load capacities within confined spaces, with an impressive power-to-volume ratio of $361 \times 10^3 \text{ W/m}^3$. They also permit the utilization of compression springs with diverse elastic properties, ensuring remarkable load bearing without elongating the actuator. Conversely, MISAs facilitate a broad spectrum of controllable stiffness in joints, a feature notably superior to that of ECAs.

The furtherance of this research through rigorous testing—encompassing high-intensity dumbbell lifting, table tennis playing, and door opening—affirms the operational efficacy and visual human resemblance of the proposed local tendon-driven actuators amalgamating both SEA and VSA designs. The success in executing complex tasks underlines the potential of these innovative compliant actuators in fostering the development of highly biomimetic robotic systems, thereby paving the way for more natural and intuitive human-robot interactions.

References

- [1] Hyon SH, Hale JG and Cheng G. Full-body compliant human–humanoid interaction: balancing in the presence of unknown external forces. *IEEE transactions on robotics* 2007; 23(5): 884–898.
- [2] Liu Y, Li Z, Su H et al. Whole body control of an autonomous mobile manipulator using series elastic actuators. *IEEE/ASME Transactions on Mechatronics* 2021; .
- [3] Pratt GA and Williamson MM. Series elastic actuators. In *Proceedings 1995 IEEE/RSJ International Conference on Intelligent Robots and Systems. Human Robot Interaction and Cooperative Robots*, volume 1. IEEE, pp. 399–406.
- [4] Schrade SO, Dätwyler K, Stücheli M et al. Development of varileg, an exoskeleton with variable stiffness actuation: first results and user evaluation from the cybathlon 2016. *Journal of neuroengineering and rehabilitation* 2018; 15: 1–18.
- [5] Shao Y, Zhang W, Su Y et al. Design and optimisation of load-adaptive actuator with variable stiffness for compact ankle exoskeleton. *Mechanism and Machine Theory* 2021; 161: 104323.
- [6] Xu Y, Guo K, Sun J et al. Design, modeling and control of a reconfigurable variable stiffness actuator. *Mechanical Systems and Signal Processing* 2021; 160: 107883.
- [7] Hussain I, Albalasie A, Awad MI et al. Design and control of a discrete variable stiffness actuator with instant stiffness switch for safe human-robot interaction. *IEEE Access* 2021; 9: 118215–118231.
- [8] Li Z, Bai S, Madsen O et al. Design, modeling and testing of a compact variable stiffness mechanism for exoskeletons. *Mechanism and Machine Theory* 2020; 151: 103905.
- [9] Engelsberger J, Werner A, Ott C et al. Overview of the torque-controlled humanoid robot toro. In *2014 IEEE-RAS International Conference on Humanoid Robots*. IEEE, pp. 916–923.
- [10] Yu Z, Huang Q, Ma G et al. Design and development of the humanoid robot bhr-5. *Advances in Mechanical Engineering* 2014; 6: 852937.
- [11] Paik JK, Shin BH, Bang Yb et al. Development of an anthropomorphic robotic arm and hand for interactive humanoids. *Journal of bionic engineering* 2012; 9(2): 133–142.
- [12] Tsagarakis NG, Li Z, Saglia J et al. The design of the lower body of the compliant humanoid robot “ccub”. In *2011 IEEE International Conference on Robotics and Automation*. IEEE, pp. 2035–2040.
- [13] Colasanto L, Tsagarakis NG and Caldwell DG. A compact model for the compliant humanoid robot coman. In *2012 4th IEEE RAS & EMBS International Conference on Biomedical Robotics and Biomechanics (BioRob)*. IEEE, pp. 688–694.
- [14] Tsagarakis NG, Caldwell DG, Negrello F et al. Walk-man: A high-performance humanoid platform for realistic environments. *Journal of Field Robotics* 2017; 34(7): 1225–1259.
- [15] Sodeyama Y, Nishino T, Namiki Y et al. The designs and motions of a shoulder structure with a spherical thorax, scapulas and collarbones for humanoid “kojiro”. In *2008 IEEE/RSJ International Conference on Intelligent Robots and Systems*. IEEE, pp. 1465–1470.
- [16] Marques HG, Jäntschi M, Wittmeier S et al. Eccel: The first of a series of anthropomimetic musculoskeletal upper torsos. In *2010 10th IEEE-RAS International Conference on Humanoid Robots*. IEEE, pp. 391–396.
- [17] Asano Y, Okada K and Inaba M. Musculoskeletal design, control, and application of human mimetic humanoid kenshiro. *Bioinspiration & biomimetics* 2019; 14(3): 036011.
- [18] Toshimitsu Y, Kawaharazuka K, Nishiura M et al. Biomimetic operational space control for musculoskeletal humanoid optimizing across muscle activation and joint nullspace. In *2021 IEEE International Conference on Robotics and Automation (ICRA)*. IEEE, pp. 1184–1190.
- [19] Fan Y, Yuan J, Wu Y et al. A feedforward compensation approach for cable-driven musculoskeletal systems. *Robotica* 2022; : 1–10.
- [20] Hyun DJ, Lim H, Park S et al. Singular wire-driven series elastic actuation with force control for a waist assistive exoskeleton, h-wexv2. *IEEE/ASME Transactions on Mechatronics* 2020; 25(2): 1026–1035.
- [21] Lee HD, Park H, Hong DH et al. Development of a series elastic tendon actuator (seta) based on gait analysis for a knee assistive exosuit. In *Actuators*, volume 11. MDPI, p. 166.
- [22] Herbin P and Pajor M. Human-robot cooperative control system based on serial elastic actuator bowden cable drive in exoarm 7-dof upper extremity exoskeleton. *Mechanism and Machine Theory* 2021; 163: 104372.

- [23] Zhu Y, Wu Q, Chen B et al. Design and evaluation of a novel torque-controllable variable stiffness actuator with reconfigurability. *IEEE/ASME Transactions on Mechatronics* 2021; 27(1): 292–303.
- [24] Nakanishi Y, Izawa T, Osada M et al. Development of musculoskeletal humanoid kenzoh with mechanical compliance changeable tendons by nonlinear spring unit. In *2011 IEEE International Conference on Robotics and Biomimetics*. IEEE, pp. 2384–2389.
- [25] Kobayashi J, Okumura K, Watanabe Y et al. Development of a variable stiffness joint drive module and experimental results of joint angle control. *Artificial Life and Robotics* 2010; 15(1): 72–76.
- [26] Mouthuy PA, Snelling S, Hostettler R et al. Humanoid robots to mechanically stress human cells grown in soft bioreactors. *Communications Engineering* 2022; 1(1): 1–11.
- [27] Kawaharazuka K, Nishiura M, Toshimitsu Y et al. Robust continuous motion strategy against muscle rupture using online learning of redundant intersensory networks for musculoskeletal humanoids. *Robotics and Autonomous Systems* 2022; 152: 104067.
- [28] Yang H, Wei G and Ren L. A novel soft actuator: Misa and its application on the biomimetic robotic arm. *IEEE Robotics and Automation Letters* 2023; 8(4): 2373–2380.
- [29] Hill AV. The heat of shortening and the dynamic constants of muscle. *Proceedings of the Royal Society of London Series B-Biological Sciences* 1938; 126(843): 136–195.
- [30] Hussain F, Goecke R and Mohammadian M. Exoskeleton robots for lower limb assistance: A review of materials, actuation, and manufacturing methods. *Proceedings of the Institution of Mechanical Engineers, Part H: Journal of Engineering in Medicine* 2021; 235(12): 1375–1385.
- [31] Zhang T, Tran M and Huang H. Admittance shaping-based assistive control of sea-driven robotic hip exoskeleton. *IEEE/ASME Transactions on Mechatronics* 2019; 24(4): 1508–1519.
- [32] Chen T, Casas R and Lum PS. An elbow exoskeleton for upper limb rehabilitation with series elastic actuator and cable-driven differential. *IEEE Transactions on Robotics* 2019; 35(6): 1464–1474.
- [33] Marconi D, Baldoni A, McKinney Z et al. A novel hand exoskeleton with series elastic actuation for modulated torque transfer. *Mechatronics* 2019; 61: 69–82.
- [34] Zhong B, Guo K, Yu H et al. Toward gait symmetry enhancement via a cable-driven exoskeleton powered by series elastic actuators. *IEEE Robotics and Automation Letters* 2021; 7(2): 786–793.
- [35] Lee C and Oh S. Development, analysis, and control of series elastic actuator-driven robot leg. *Frontiers in neurorobotics* 2019; 13: 17.
- [36] Hong C, Tang D, Quan Q et al. A combined series-elastic actuator & parallel-elastic leg no-latch bio-inspired jumping robot. *Mechanism and Machine Theory* 2020; 149: 103814.
- [37] Zhu Q, Mao Y, Xiong R et al. Adaptive torque and position control for a legged robot based on a series elastic actuator. *International Journal of Advanced Robotic Systems* 2016; 13(1): 26.
- [38] Accoto D, Carpino G, Sergi F et al. Design and characterization of a novel high-power series elastic actuator for a lower limb robotic orthosis. *International Journal of Advanced Robotic Systems* 2013; 10(10): 359.
- [39] Pratt JE and Krupp BT. Series elastic actuators for legged robots. In *Unmanned Ground Vehicle Technology VI*, volume 5422. SPIE, pp. 135–144.
- [40] Sun X, Sugai F, Okada K et al. Variable transmission series elastic actuator for robotic prosthesis. In *2018 IEEE International Conference on Robotics and Automation (ICRA)*. IEEE, pp. 2796–2803.
- [41] Convens B, Dong D, Furnémont R et al. Modeling, design and test-bench validation of a semi-active propulsive ankle prosthesis with a clutched series elastic actuator. *IEEE Robotics and Automation Letters* 2019; 4(2): 1823–1830.
- [42] Rouse EJ, Mooney LM and Herr HM. Clutchable series-elastic actuator: Implications for prosthetic knee design. *The International Journal of Robotics Research* 2014; 33(13): 1611–1625.
- [43] Knabe C, Seminatore J, Webb J et al. Design of a series elastic humanoid for the darpa robotics challenge. In *2015 IEEE-RAS 15th International Conference on Humanoid Robots (Humanoids)*. IEEE, pp. 738–743.
- [44] Yu H, Huang S, Chen G et al. Human–robot interaction control of rehabilitation robots with series elastic actuators. *IEEE Transactions on Robotics* 2015; 31(5): 1089–1100.
- [45] Yu H, Huang S, Thakor NV et al. A novel compact compliant actuator design for rehabilitation robots. In *2013 IEEE 13th international conference on rehabilitation robotics (ICORR)*. IEEE, pp. 1–6.

- [46] Kong K, Bae J and Tomizuka M. Control of rotary series elastic actuator for ideal force-mode actuation in human–robot interaction applications. *IEEE/ASME transactions on mechatronics* 2009; 14(1): 105–118.
- [47] Ragonesi D, Agrawal S, Sample W et al. Series elastic actuator control of a powered exoskeleton. In *2011 Annual International Conference of the IEEE Engineering in Medicine and Biology Society*. IEEE, pp. 3515–3518.
- [48] Paine N and Sentis L. A new prismatic series elastic actuator with compact size and high performance. In *2012 IEEE International Conference on Robotics and Biomimetics (ROBIO)*. IEEE, pp. 1759–1766.
- [49] Truong KD, Luu AKL, Tong NP et al. Design of series elastic actuator applied for humanoid. In *2020 International Conference on Advanced Mechatronic Systems (ICAMechS)*. IEEE, pp. 23–28.
- [50] Lu J, Haninger K, Chen W et al. Design and torque-mode control of a cable-driven rotary series elastic actuator for subject-robot interaction. In *2015 IEEE International Conference on Advanced Intelligent Mechatronics (AIM)*. IEEE, pp. 158–164.
- [51] Magid A and Law DJ. Myofibrils bear most of the resting tension in frog skeletal muscle. *Science* 1985; 230(4731): 1280–1282.
- [52] Tsagarakis NG, Laffranchi M, Vanderborght B et al. A compact soft actuator unit for small scale human friendly robots. In *2009 IEEE international conference on robotics and automation*. IEEE, pp. 4356–4362.
- [53] Wolf S, Eiberger O and Hirzinger G. The dlr fsj: Energy based design of a variable stiffness joint. In *2011 IEEE international conference on robotics and automation*. IEEE, pp. 5082–5089.
- [54] Guo J and Tian G. Mechanical design and analysis of the novel 6-dof variable stiffness robot arm based on antagonistic driven joints. *Journal of Intelligent & Robotic Systems* 2016; 82(2): 207–235.
- [55] Thorson I and Caldwell D. A nonlinear series elastic actuator for highly dynamic motions. In *2011 IEEE/RSJ International Conference on Intelligent Robots and Systems*. IEEE, pp. 390–394.
- [56] Wolf S and Hirzinger G. A new variable stiffness design: Matching requirements of the next robot generation. In *2008 IEEE International Conference on Robotics and Automation*. IEEE, pp. 1741–1746.
- [57] Tonietti G, Schiavi R and Bicchi A. Design and control of a variable stiffness actuator for safe and fast physical human/robot interaction. In *Proceedings of the 2005 IEEE international conference on robotics and automation*. Barcelona, Spain: IEEE, pp. 526–531.
- [58] Schiavi R, Grioli G, Sen S et al. Vsa-ii: A novel prototype of variable stiffness actuator for safe and performing robots interacting with humans. In *2008 IEEE International Conference on Robotics and Automation*. IEEE, pp. 2171–2176.
- [59] Palli G, Berselli G, Melchiorri C et al. Design of a variable stiffness actuator based on flexures. *Journal of Mechanisms and Robotics* 2011; .
- [60] Qian Y, Han S, Aguirre-Ollinger G et al. Design, modeling, and control of a reconfigurable rotary series elastic actuator with nonlinear stiffness for assistive robots. *Mechatronics* 2022; 86: 102872.
- [61] Toubar H, Awad MI, Boushaki MN et al. Design, modeling, and control of a series elastic actuator with discretely adjustable stiffness (seadas). *Mechatronics* 2022; 86: 102863.
- [62] Abe K, Suga T and Fujimoto Y. Control of a biped robot driven by elastomer-based series elastic actuator. In *2012 12th IEEE International Workshop on Advanced Motion Control (AMC)*. IEEE, pp. 1–6.
- [63] Yildirim MC, Sendur P, Kansizoglu AT et al. Design and development of a durable series elastic actuator with an optimized spring topology. *Proceedings of the Institution of Mechanical Engineers, Part C: Journal of Mechanical Engineering Science* 2021; 235(24): 7848–7858.
- [64] Chen B, Zhao X, Ma H et al. Design and characterization of a magneto-rheological series elastic actuator for a lower extremity exoskeleton. *Smart Materials and Structures* 2017; 26(10): 105008.
- [65] Mori S, Tanaka K, Nishikawa S et al. High-speed humanoid robot arm for badminton using pneumatic-electric hybrid actuators. *IEEE Robotics and Automation Letters* 2019; 4(4): 3601–3608.
- [66] Sakagami Y, Watanabe R, Aoyama C et al. The intelligent asimo: System overview and integration. In *IEEE/RSJ international conference on intelligent robots and systems*, volume 3. IEEE, pp. 2478–2483.
- [67] Ogura Y, Aikawa H, Shimomura K et al. Development of a new humanoid robot wabian-2. In *Proceedings 2006 IEEE International Conference on Robotics and Automation, 2006. ICRA 2006*. IEEE, pp. 76–81.
- [68] Xia Z, Liu L, Xiong J et al. Design aspects and development of humanoid robot thbip-2. *Robotica* 2008; 26(1): 109–116.

- [69] Nichols RK, Carter CM, Drew II JV et al. Artificial brains and body [mumm]. *Cyber-Human Systems, Space Technologies, and Threats* 2023; .
- [70] Ackerman E and Guizzo E. What robotics experts think of tesla’s optimus robot. *IEEE Spectrum* 2022; 4.
- [71] Haines CS, Lima MD, Li N et al. Artificial muscles from fishing line and sewing thread. *science* 2014; 343(6173): 868–872.
- [72] Lu X, Ren L, Wang K et al. Reproduction of the mechanical behavior of ligament and tendon for artificial joint using bioinspired 3d braided fibers. *IEEE Transactions on Neural Systems and Rehabilitation Engineering* 2022; 30: 1172–1180.
- [73] Sheikhzadeh A, Yoon J, Pinto VJ et al. Three-dimensional motion of the scapula and shoulder during activities of daily living. *Journal of Shoulder and Elbow Surgery* 2008; 17(6): 936–942.
- [74] Senoo T, Namiki A and Ishikawa M. Ball control in high-speed batting motion using hybrid trajectory generator. In *Proceedings 2006 IEEE International Conference on Robotics and Automation, 2006. ICRA 2006*. IEEE, pp. 1762–1767.
- [75] Paine N, Oh S and Sentis L. Design and control considerations for high-performance series elastic actuators. *IEEE/ASME Transactions on Mechatronics* 2013; 19(3): 1080–1091.
- [76] Lee B, Orekhov V, Lahr D et al. Design and measurement error analysis of a low-friction, lightweight linear series elastic actuator. In *International Design Engineering Technical Conferences and Computers and Information in Engineering Conference*, volume 55942. American Society of Mechanical Engineers, p. V06BT07A022.
- [77] Knabe C, Lee B, Orekhov V et al. Design of a compact, lightweight, electromechanical linear series elastic actuator. In *International Design Engineering Technical Conferences and Computers and Information in Engineering Conference*, volume 46377. American Society of Mechanical Engineers, p. V05BT08A014.
- [78] Pratt J, Krupp B and Morse C. Series elastic actuators for high fidelity force control. *Industrial Robot: An International Journal* 2002; 29(3): 234–241.
- [79] Kong K, Bae J and Tomizuka M. A compact rotary series elastic actuator for human assistive systems. *IEEE/ASME transactions on mechatronics* 2011; 17(2): 288–297.
- [80] Sergi F, Accoto D, Carpino G et al. Design and characterization of a compact rotary series elastic actuator for knee assistance during overground walking. In *2012 4th IEEE RAS & EMBS International Conference on Biomedical Robotics and Biomechatronics (BioRob)*. IEEE, pp. 1931–1936.
- [81] Agarwal P and Deshpande AD. Series elastic actuators for small-scale robotic applications. *Journal of Mechanisms and Robotics* 2017; 9(3): 031016.
- [82] Agarwal P, Fox J, Yun Y et al. An index finger exoskeleton with series elastic actuation for rehabilitation: Design, control and performance characterization. *The International Journal of Robotics Research* 2015; 34(14): 1747–1772.